

NEW CONSTRAINTS ON THE QUASAR BROAD EMISSION LINE REGION

ANDREA J. RUFF¹, DAVID J. E. FLOYD^{1,2}, RACHEL L. WEBSTER¹, KIRK T. KORISTA³, AND HERMINE LANDT¹

¹ School of Physics, University of Melbourne, Parkville, VIC 3010, Australia; aruff@unimelb.edu.au

² School of Physics, Monash University, VIC 3800, Australia

³ Department of Physics, Western Michigan University, Kalamazoo, MI 49008, USA

Received 2011 December 14; accepted 2012 May 14; published 2012 June 29

ABSTRACT

We demonstrate a new technique for determining the physical conditions of the broad-line-emitting gas in quasars, using near-infrared hydrogen emission lines. Unlike higher ionization species, hydrogen is an efficient line emitter for a very wide range of photoionization conditions, and the observed line ratios depend strongly on the density and photoionization state of the gas present. A locally optimally emitting cloud model of the broad emission line region was compared to measured emission lines of four nearby ($z \approx 0.2$) quasars that have optical and NIR spectra of sufficient signal to noise to measure their Paschen lines. The model provides a good fit to three of the objects, and a fair fit to the fourth object, an ultraluminous infrared galaxy. We find that low-incident-ionizing fluxes ($\Phi_{\text{H}} < 10^{18} \text{ cm}^{-2} \text{ s}^{-1}$) and high gas densities ($n_{\text{H}} > 10^{12} \text{ cm}^{-3}$) are required to reproduce the observed hydrogen emission line ratios. This analysis demonstrates that the use of composite spectra in photoionization modeling is inappropriate; models must be fitted to the individual spectra of quasars.

Key words: galaxies: active – infrared: galaxies – quasars: emission lines

Online-only material: color figures

1. INTRODUCTION

Physical models of the broad emission line region (BELR) of active galactic nuclei (AGNs) have been frustrated by the complexity of the expected emission mechanisms, and a poor understanding of the physical state, dynamics, and spatial distribution of the line-emitting gas. Innovative new techniques, including reverberation mapping (Peterson 1994) and microlensing (e.g., O’Dowd et al. 2011; Bate et al. 2008), are providing indirect methods to measure the physical sizes of the emission regions. To date, each of these techniques has only been applied to a select sample of sources. However, useful models of the BELR will require constraints on all physical parameters. Broad emission line fluxes provide a powerful diagnostic of the physical conditions in the BELR, particularly when coupled with photoionization simulations from codes, such as Cloudy.

Broad emission lines are a prominent feature in luminous AGNs, and a defining characteristic of quasars. These emission lines are typically broadened by gas velocities of $\sim 10^4 \text{ km s}^{-1}$, and are understood to arise from gas close to the central black hole and its accretion disk. The broad emission line gas reprocesses a substantial amount of the light emitted from the central region. The emitted line fluxes, and in particular their ratios, are strongly dependent on the local physical conditions. The BELR is the closest material that interacts strongly with the accretion disk that can be probed observationally, and a detailed physical understanding is essential in understanding the role of AGN energy injection at larger scales.

A compact BELR has been inferred from reverberation mapping (e.g., Blandford & McKee 1982; Peterson 1994). As a result of the small spatial scale of the BELR and large distances to the nearest quasars, direct spatial imaging of the BELR is not possible. In the absence of detailed structural information, we can develop photoionization models to predict spectral line ratios and infer the properties of the emitting gas. Such calculations are particularly sensitive to the density and ionization state of the gas (e.g., Davidson 1972; Osterbrock &

Mathews 1986). This provides an alternative estimate of the physical scale of the BELR.

Early BELR photoionization simulations were limited to single cloud models with a single number density, column density, and ionization parameter. Simulating the entire range of possible BELR parameter space was not possible, due to computational limitations. These simulations were reasonably successful in reproducing a number of observed emission line flux ratios (e.g., Davidson 1977; Kwan & Krolik 1981). However, as more spectroscopic data became available, there was conflicting evidence: On one hand, the presence of semi-forbidden transitions, such as C III] $\lambda 1909$ suggested reasonably low number density gas (Osterbrock 1970), while the hydrogen emission line ratios and strong Fe II emission suggested the presence of high number density gas (e.g., Rees et al. 1989; Collin-Souffrin et al. 1982). Broad emission line continuum reverberation measurements find a wide range in emission line lags relative to the continuum variations and line widths, arguing for a distributed geometry of physical conditions (e.g., see Krolik et al. 1991; Peterson 2011). To reconcile these conflicting observations, Baldwin et al. (1995) proposed a locally optimally emitting cloud (LOC) model, where gas “clouds” with a range of physical properties exist at each radius in a spatially extended BELR. This model takes advantage of large grids of photoionization models that can now be simulated over a huge range of parameter space in the density–flux plane (Korista et al. 1997).

The LOC model has been successful in producing ultraviolet and optical emission line flux ratios that match observations (Baldwin et al. 1995; Korista & Goad 2000; Bottorff et al. 2000), while maintaining consistency with reverberation mapping results (e.g., Korista & Goad 2004). The LOC also provides an explanation for the remarkably consistent BELR flux ratios, over a very large range in AGN luminosity. The name, “LOC” originated because many of the optical and ultraviolet (UV) broad emission lines emit “optimally” in one region in parameter space. Specifically, the typical emission line is efficiently emitted (relative to the incident continuum) over a relatively

narrow region within the density–incident continuum flux plane (see Figure 1 of Baldwin et al. 1995). This natural selection effect is due to a combination of ionization potential, collisional de-excitation of the upper level, and thermalization at large optical depths. Reverberation mapping measurements show that individual emission lines respond to variations in the continuum with different time delays, and the characteristic radius where each line is produced depends on the ionization potential (i.e., high-ionization lines are emitted closer to the continuum source). The term, “LOC,” is less appropriate for the H I and He I lines, as the production of these lines from the continuum remains efficient over a large range of the density–flux plane (Korista et al. 1997; A. J. Ruff et al. 2012, in preparation).

The hydrogen and helium lines are of particular interest because the physical processes governing their production is relatively simple, and there is a negligible dependence on several free parameters of the model: metallicity, column density, and slope of the ionizing continuum. Despite the relative simplicity of the H I emission spectrum, some unexplained observations persist, such as the Ly α /H β problem (Baldwin 1977; Netzer et al. 1995) and the small scatter in measured Balmer decrements (H α /H β) of AGNs with blue continua (Dong et al. 2008). The simple recombination spectrum predictions of Case B are invalid for several reasons under BELR conditions. First, given the high gas number density, high-incident flux environment, the optical depths in the Balmer and Paschen lines are finite and often large. Second, the effects of collisions are expected to be very important, especially in light of the enhanced lifetime of the $n = 2$ state due to the enormous Ly α optical depths that are encountered.

Although the LOC model has been shown to produce emission line flux ratios that are consistent with measured emission lines for optical and UV metal emission lines (Baldwin et al. 1995; Korista & Goad 2000) as well as helium emission lines (Bottorff et al. 2002; Korista & Goad 2004), no comprehensive study of the infrared hydrogen lines has been undertaken. The near-infrared (NIR) lines, for example, the hydrogen Paschen series, have the advantage of being affected by dust equally, whereas there is differential extinction across the optical and UV lines. With advances in infrared spectroscopy, larger samples of both low-luminosity AGNs (Landt et al. 2008) and higher-luminosity quasars (Glikman et al. 2006) are being observed. The Paschen lines are becoming more widely used for AGN measurements, such as black hole mass (e.g., Kim et al. 2010).

This paper investigates a new diagnostic that tests the LOC model using near-infrared hydrogen emission lines in quasars. The narrow component has a larger contribution to the total line flux in lower-luminosity AGNs, and the systematic uncertainties resulting from this subtraction must be quantified. We have concentrated on quasars (as opposed to Seyferts and other lower-luminosity AGNs), so that deconvolution of the emission lines into broad and narrow components is not necessary. We use only spectra of individual objects, and demonstrate that composite spectra are not suitable for determining the physical conditions in quasars. Section 2 describes the photoionization simulations and the simple LOC model used in this analysis. Section 3 describes data used. Measurements are compared to the LOC model in Section 4. A discussion of the results is given in Section 5, before a brief summary in Section 6.

2. PHOTOIONIZATION MODELS

Following the standard LOC approach (Baldwin et al. 1995; Korista et al. 1997; Korista & Goad 2000), a large grid of

photoionization models was computed using the photoionization code, Cloudy version 08.00, last described by Ferland et al. (1998). Version 08.00 of Cloudy implemented full resolution of quantum l -levels⁴ for the H- and He-like sequences for the first time (Ferguson & Ferland 1997; Ferguson et al. 2001; Porter et al. 2005; Porter & Ferland 2007), greatly improving the accuracy of the predicted emission. For greater predictive accuracy, the number of resolved quantum levels in the H I and He I atoms was increased from the Cloudy defaults.⁵ A brief outline of the grid simulations is given below. A more detailed description of the photoionization simulations is given by A. J. Ruff et al. (2012, in preparation).

In the context of an LOC model, the term, “cloud” refers to an individual emitting body of gas within the BELR. Emission line profiles are observed to be very smooth, implying either a large number of clouds (Arav et al. 1998), or a smoothing mechanism. Micro-turbulence of $\sim 100 \text{ km s}^{-1}$ would broaden the local line profile sufficiently to smooth the bulk line profile to match the observed (e.g., as mentioned in Arav et al. 1998; see also Bottorff et al. 2000; Kollatschny & Zetzl 2011). Micro-turbulence also reproduces the observed UV Fe II bump (Baldwin et al. 2004). The presence of a small amount of electron scattering (e.g., Emmering et al. 1992; Laor 2006) or macro-turbulence in the cloud velocity field could also smooth the profile. The precise nature of the line-emitting entities is not the focus of this investigation. Instead we focus on constraining general physical conditions of the emitting gas using hydrogen emission line flux ratios.

2.1. Grid Simulations in the Density–Flux Plane

Models that predict hydrogen and helium emission line strengths were generated for a range of hydrogen number density (n_{H}) and hydrogen ionizing flux (Φ_{H}) values. The plane formed by these parameters represents the range of cloud densities and distances from the ionizing continuum that are expected to exist within the BELR. The output emission of the photoionization simulations is computed as an equivalent width in angstroms relative to the incident continuum at 1216 Å (W_{1216}). The equivalent width is a useful description of the line emission, as it measures how efficiently the line is produced from the incident continuum.

For each point in the grid, Cloudy’s standard AGN-ionizing continuum (similar to the Mathews & Ferland 1987 continuum) was used. Despite a range in observed ionizing continua, the H and He emission lines are relatively insensitive to the shape of the ionizing continuum, unlike the metal emission lines (Korista et al. 1997). A constant number density within each cloud was assumed and a constant column density of $N_{\text{H}} = 10^{23} \text{ cm}^{-2}$ was also assumed. Although a range of column densities is expected within the BELR, the hydrogen and helium emission lines are not very sensitive to the cloud column density in the range $10^{22} < N_{\text{H}}(\text{cm}^{-2}) < 10^{24}$ (Korista et al. 1997; A. J. Ruff et al. 2012, in preparation). Note that solar chemical abundances were used for all photoionization simulations.

2.2. Limits on the Number Density, Ionizing Flux, and Ionization Parameter

The range of values for each of the physical parameters in the LOC model is motivated by observations and physical

⁴ The azimuthal quantum number, l , is one of the numbers that describes the quantum state of an electron.

⁵ Simulations used H I and He I model atoms with 18 and 15 resolved levels, respectively.

considerations. Broad, semi-forbidden C III] λ 1909 is observed, implying the presence of $\sim 10^9 \text{ cm}^{-3}$ gas (Davidson & Netzer 1979), as it is collisionally suppressed at higher densities. However, broad forbidden lines are not observed, indicating that the electron density in the BELR is higher than the critical density of the forbidden lines. This gives a lower limit on the number density within the BELR and only clouds with $n_H > 10^7 \text{ cm}^{-3}$ were considered. While none of the broad emission lines can be used to determine an upper limit on the number density, analyses of the Balmer lines, whose ratios are sensitive to high-density gas, and strong Fe II emission indicate that high-density ($\sim 10^{12} \text{ cm}^{-3}$) gas is also present within the BELR (e.g., Collin-Souffrin et al. 1982; Rees et al. 1989). At these high densities, collisional excitation becomes important. The collisional excitation depends on density, temperature, and ionization state in a fundamentally different manner to the recombination Case B (Ferland et al. 2009). Therefore, detailed photoionization simulations are required.

Reverberation mapping measurements show that broad emission lines originate at a range of radii from the central ionizing source (Peterson 1994). At large distances from the continuum source, the ionizing flux is low and the temperature decreases. Below temperatures of $\sim 1500 \text{ K}$ dust grains condense, making the line emissivity low (e.g., Netzer & Laor 1993). This temperature corresponds to a hydrogen ionizing flux of $\Phi_H \sim 10^{18} \text{ cm}^{-2} \text{ s}^{-1}$ (Nenkova et al. 2008, after substituting a fiducial bolometric luminosity). The H I and He I emissivities are strongly dependent on the incident ionizing flux, unlike most of the prominent metal lines (Korista & Goad 2004). This is because the optical depth of the H I and He I excited states increases with ionizing flux (Ferland et al. 1979, 1992), until the cloud is fully ionized. Close to the ionizing source, the hydrogen and helium atoms will be fully ionized and will not produce line emission. As the H I and He I line emissivity is low at large Φ_H values, the upper limit on Φ_H is considered to be unimportant.

Considering the limits discussed above, a large range in BELR parameter space was simulated, spanning seven decades in both n_H and Φ_H : $10^7 \leq n_H (\text{cm}^{-3}) \leq 10^{14}$ and $10^{17} \leq \Phi_H (\text{cm}^{-2} \text{ s}^{-1}) \leq 10^{24}$, each stepped in 0.25 decade intervals. Each model was calculated separately by Cloudy, giving a total of 841 photoionization calculations. Contour plots of each line, showing the W_{1216} as a function of n_H and Φ_H will be presented in A. J. Ruff et al. (2012, in preparation). A lower limit on the ionization parameter,

$$U \equiv \frac{\Phi_H}{c n_H}, \quad (1)$$

was also considered. This is motivated by observations of the calcium infrared triplet, Ca II XYZ $\lambda\lambda$ 8498, 8542, 8662. If clouds with very low values of the ionization parameter ($\log U \leq -6$) existed in the BELR, stronger Ca II XYZ (Joly 1989; Ferland & Persson 1989) and Na I λ 5895 emission would be observed (see Korista et al. 1997, for a range of W_{1216} distributions in the density–flux plane). In addition, the Fe II emission would be totally dominated by resonance transitions clustered near 2400 \AA and 2600 \AA (Verner et al. 1999), which is dissimilar to the pseudocontinuum observed. A physical interpretation of the lower limit on the ionization parameter, U_{\min} is that very dense clouds are not found far from the ionizing continuum. Although this limit may not exactly represent the true physical cloud distribution, it is a convenient representation in the LOC model.

These considerations provide only weak constraints on the upper n_H limit, and lower Φ_H and U_{\min} limits in the BELR. However, they are very important because of the large emissivity of H I and He I close to these limits. The H I and He I line ratios are particularly sensitive to the lower Φ_H and upper n_H values (Φ_{\min} and n_{\max} , respectively). Thus, rather than using fiducial values, a range of upper and lower limits on Φ_H and n_H was considered.

2.3. Calculating the Total Equivalent Width

Following the standard LOC prescription, the flux from each point in the simulated parameter space was summed to calculate the emission from each species of interest. As shown by Baldwin et al. (1995), the line luminosity is given by

$$L_{\text{line}} \propto \int_{r_{\min}}^{r_{\max}} \int_{n_{\min}}^{n_{\max}} W_{1216}(r, n_H) f(r) g(n_H) dn_H dr, \quad (2)$$

where $W_{1216}(r, n_H)$ is the equivalent width of a particular line (relative to the continuum at 1216 \AA) from a single cloud at radius r , with number density n_H . The cloud covering fractions as functions of radius and number density are given by $f(r)$ and $g(n_H)$, respectively. For a more complete description of the LOC parameters, see Bottorff et al. (2002). In the simplest case of LOC integration, the covering fractions are given by $f(r) \propto r^{-1}$ and $g(n_H) \propto n_H^{-1}$ (Baldwin et al. 1995; see also Matsuoka et al. 2007). The line luminosity can then be simplified to

$$L_{\text{line}} \propto \int_{\log \Phi_{\min}}^{\log \Phi_{\max}} \int_{\log n_{\min}}^{\log n_{\max}} W_{1216}(\Phi_H, n_H) d \log n_H d \log \Phi_H, \quad (3)$$

where the integration limits are free parameters of the model and $\Phi_H \propto r^{-2}$. This is simply a sum over each point in parameter space between the integration limits, since the simulated photoionized clouds in the logarithmic grid are weighted evenly per decade. We note that this weighting scheme maximizes the distribution of cloud characteristics in gas density and incident ionizing flux—a key characteristic of the LOC model. Power-law indices in the density and distance weighting functions ($f(r)$, $g(n_H)$) that deviate substantially from -1 will take on characteristics of a model with a single gas density and ionizing continuum source distance.⁶

This sum (Equation (3)) then allows us to compute the predicted total equivalent width (W_{1216}) for each emission line, assuming full geometric coverage. The model-integrated covering fraction is then determined from the ratio between the observed $W_{1216}(\text{Ly}\alpha)$ and its predicted value, above. While in the present work we are mainly interested in comparing hydrogen Balmer and Paschen emission line flux ratios (which are independent of the integrated covering fraction), Table 5 lists the value of the integrated covering fraction that results in a predicted equivalent width of $\text{Ly}\alpha$ of 100 \AA , a typical value (see also Section 4.4).

2.4. Ratios Calculated from Varying the Integration Limits

Broad emission line flux ratios were predicted for several emission line pairs using Equation (3). Rather than using fiducial

⁶ In studies of the UV emission lines in NGC 5548 (Korista & Goad 2000) and SDSS quasars (Nagao et al. 2006), there is evidence for favoring adoption of a slightly steeper power-law index in $f(r)$, which tends to favor gas at smaller distances from the central continuum source. Here, however, given the limited number of observational constraints (discussed in Section 3), we choose to adopt the simplest weighting scheme in the LOC integration.

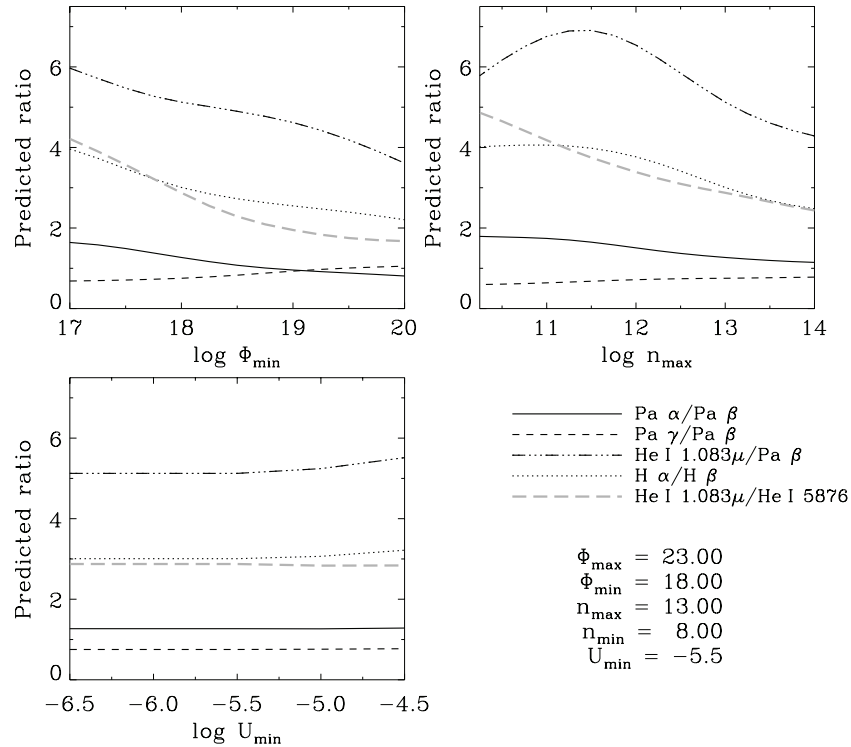


Figure 1. Flux ratios are shown as a function of varying three integration limits: Φ_{\min} , n_{\max} , and U_{\min} . Each panel shows the variation of a different limit, while the other limits are held at constant at fiducial values, given in the legend.

values of the integration limits to predict ratios, a range of upper and lower bounds on each of the free parameters: Φ_{\min} , n_{\max} , and U_{\min} was considered. From the discussion in Section 2.2, the Φ_{\min} , n_{\max} , and U_{\min} integration limits were varied over the ranges

$$\begin{aligned} \log \Phi_{\min} &= [17.00, 20.00] \\ \log n_{\max} &= [10.25, 14.00] \\ \log U_{\min} &= [-6.5, -4.5] \end{aligned} \quad (4)$$

To limit the number of assumptions in the calculation, these integration limits span a larger range than suggested by the observational limits discussed in Section 2.2. The Φ_{\min} and n_{\max} integration limits were stepped in 0.25 decade intervals and the U_{\min} limit in 0.5 decade intervals. The Φ_{\max} and n_{\min} limits were also varied, however the effect on the total emission was small, because the H I and He I lines have low emissivity in this region of parameter space. The values of Φ_{\max} and n_{\min} were fixed at $10^{23} \text{ cm}^{-2} \text{ s}^{-1}$ and 10^8 cm^{-3} , respectively. The change in predicted ratio caused by varying these limits was less than 1%.

To visualize how the ratios change as the Φ_{\min} , n_{\max} , and U_{\min} integration limits are varied, several flux ratios are plotted against each of the integration limits. Figure 1 plots several predicted ratios: $\text{Pa } \alpha / \text{Pa } \beta$, $\text{Pa } \gamma / \text{Pa } \beta$, $\text{He I } 1.083\mu / \text{Pa } \beta$, $\text{H } \alpha / \text{H } \beta$, and $\text{He I } 1.083\mu / \text{He I } \lambda 5876$ as a function of Φ_{\min} , n_{\max} , and U_{\min} integration limits. The three panels show ratios plotted as a function of each of the integration limits over the range given in Equation (4), while the other integration limits are held constant at fiducial values (given in the legend).

3. APPLICATION TO DATA

Very few quasars have been observed in the infrared with high signal to noise. Glikman et al. (2006) published a set of 27 low signal-to-noise quasar spectra, which was presented

as a composite quasar spectrum. Averaging quasar spectra is complicated by several factors that limit the accuracy of emission line fluxes measured from the composite spectrum, see Section 5.3 for details.

Rather than using the composite spectrum, individual spectra with the highest signal-to-noise ratios (S/N) from Glikman et al. (2006) were analyzed. In practice our cutoff was $\text{S/N} > 10 \text{ pixel}^{-1}$ in the continuum between the $\text{Pa } \alpha$ and $\text{Pa } \beta$ emission lines (excluding any regions of significant atmospheric absorption). Although there have been other NIR observations of Seyferts (Landt et al. 2008), only quasars were studied, as the subtraction of a significant narrow component in Seyfert galaxies adds additional uncertainty, which must be quantified in order to compare measured to predicted line fluxes.

3.1. Measured Broad Emission Line Fluxes

Four quasar spectra from the Glikman et al. (2006) sample have high enough S/Ns to measure the strongest Paschen emission line fluxes. For each emission line in the Sloan Digital Sky Survey (SDSS) and Glikman et al. spectra, the local continuum was measured over a wavelength range ± 200 to 500 \AA , centered on the line's expected wavelength. Linear fits to the continuum were performed after removing the line itself and any 2σ outliers. To measure line strengths, both Gaussian fits and simple integrations of the flux per wavelength bin were performed for each line. While Gaussians are an imperfect match to the line shapes, they minimize parameterization while allowing for de-blending of the He I and Pa γ lines. Integrating the flux per wavelength bin over ± 2 FWHM reproduced the Gaussian line fluxes within the errors. Summing over ± 3 FWHM admits smaller outlying features and so tends to result in an overestimate of the line strength. Measured line fluxes are shown in Table 1 together with their 1σ measurement uncertainties. The

Table 1
Measured NIR and Optical Line Fluxes

Object	He I 5876 Å		H γ 4341 Å		H β 4861 Å		H α 6563 Å		He I 1.083 μ m		Pa γ 1.094 μ m		Pa β 1.282 μ m		Pa α 1.876 μ m	
	<i>F</i>	$\epsilon(F)$	<i>F</i>	$\epsilon(F)$	<i>F</i>	$\epsilon(F)$	<i>F</i>	$\epsilon(F)$	<i>F</i>	$\epsilon(F)$	<i>F</i>	$\epsilon(F)$	<i>F</i>	$\epsilon(F)$	<i>F</i>	$\epsilon(F)$
J005812+160201	347	10%	1285	10%	4364	10%	11446	10%	1580	14%	626	17%	1078	14%	1388	12%
J010226–003904	630	11%	2577	10%	6281	10%	18003	10%	2776	11%	1264	10%	1370	10%	1661	10%
J015950+002340 ^a	2452	10%	4259	10%	7506	10%	13447	50%	5222	10%	1296	11%	2100	11%	2772	11%
J032213+005513	682	10%	3883	10%	7888	10%	22781	10%	2202	11%	1151	11%	1779	10%	2421	11%

Notes. Measured NIR and optical line fluxes (10^{-17} erg s $^{-1}$ cm $^{-2}$) with their associated measurement uncertainties. The optical lines: H α , H β , H γ , and He I λ 5876 were measured directly from the SDSS spectra, and have been scaled by f_{SDSS} from Table 2 for comparison with the infrared lines. A 10% systematic uncertainty was estimated on each emission line flux, predominantly due to the use of Gaussian fitting (see the text). J015950+002340^a is a ULIRG with an extremely asymmetric H α line; the 50% error on H α accounts for the inadequacy of a Gaussian fit for this line.

Table 2
Observables, Flux Matching, and Estimates of the 1216 Å and 5100 Å Continuum Fluxes

Object	<i>z</i>	GALEX				SDSS			
		<i>S</i> _{FUV}	<i>S</i> _{NUV}	<i>E</i> _{B–V}	<i>S</i> ₁₂₁₆	<i>S</i> ₁₂₁₆	<i>S</i> ₅₁₀₀	<i>f</i> _{SDSS}	$\epsilon(f_{\text{SDSS}})$
SDSSJ005812.8+160201.3	0.211	...	20.6	0.075	...	110	42	0.729	1.2%
SDSSJ010226.3–003904.6	0.295	880	431	0.036	2300	2200	130	1.452	0.6%
SDSSJ015950.2+002340.8	0.163	1020	580	0.029	2500	2600	170	1.073	0.6%
SDSSJ032213.8+005513.4	0.185	164	108	0.120	790	1100	100	1.003	0.8%

Notes. SDSS target name; redshift; *GALEX* raw observed fluxes (10^{-17} erg s $^{-1}$ cm $^{-2}$ Å $^{-1}$) at 1516 ± 134 Å (FUV) and 2267 ± 366 Å (NUV); Galactic extinction color excess (Schlegel et al. 1998); *GALEX* estimate of continuum flux at 1216 Å; SDSS-extrapolated continuum flux at 1216 Å and measured continuum at 5100 Å; flux factor to match SDSS to the NIR spectra and its uncertainty, ϵ . Note that *GALEX* *S*_{FUV} and *S*_{NUV} fluxes have not been corrected for extinction in this table.

SDSS line strengths were scaled by f_{SDSS} to allow direct comparison. An additional 10% systematic error was conservatively added in quadrature to measurement errors in all figures and calculations.

3.2. Measured Continuum Fluxes

For each of the four objects in the sample, SDSS spectra and *Galaxy Evolution Explorer* (*GALEX*) ultraviolet flux measurements were obtained from archival data. Color excess values, $E(B - V)$ (Schlegel et al. 1998) are given in Table 2, and these were used to correct all the data for Galactic extinction following Fitzpatrick (1999). Note that although the continuum fluxes inferred in this section have large uncertainties, the inferred physical conditions do not depend on these values. The measured continuum flux values are only used in Section 4.4 to check that the model produces enough energy to be consistent with previous observations.

For each object, the continuum level of the SDSS spectrum was scaled to match the NIR continuum across the region of overlap. The scaling factor for each SDSS spectrum, denoted f_{SDSS} , was typically measured to better than 2% accuracy. The continuum flux at 5100 Å (*S*₅₁₀₀) was measured from the SDSS spectrum, which can be scaled to match the NIR data using f_{SDSS} . An extrapolation of the best linear fit to the optical continuum was made to give an estimate of the rest-frame 1216 Å continuum flux (*S*₁₂₁₆(SDSS)). *S*₁₂₁₆(SDSS) is likely to overestimate the true continuum flux at 1216 Å due to the turnover in the spectrum. An alternative estimate of the 1216 Å continuum flux was obtained from the *GALEX* far-ultraviolet (FUV) measurement. Due to the shape, breadth, and variable position of Ly α in the *GALEX* bandpass for our sample, we cannot use the equivalent width of Ly α alone to estimate the 1216 Å continuum flux. Instead we convolve an appropriately redshifted composite quasar spectrum (Vanden Berk et al. 2001) with the *GALEX* FUV bandpass to estimate the continuum level.

The SDSS and *GALEX* estimates of the 1216 Å continuum flux level are in good agreement, considering the significant uncertainty in extrapolating the continuum. Figure 2 shows the NIR spectra, scaled SDSS spectra, and *GALEX* photometry.

4. RESULTS

The primary aim of this paper is to find a set of integration limits for the hydrogen number density and hydrogen ionizing flux (see Equation (3)) that best fit the measured infrared hydrogen emission line ratios for individual quasars. Since there are only a few measured infrared ratios, only a small number of model free parameters can be fitted. Thus, the aim of this analysis is to illustrate the potential of using optical and infrared hydrogen and helium emission lines as probes of the physical conditions within the BELR, rather than constraining a definitive model.

4.1. Best-fit Integration Limits

A set of “best-fit” integration limits was found for each object using the measured Pa α /Pa β , Pa γ /Pa β , and H α /Pa β ratios. Ratios involving optical emission lines were not used, as they suffer differential extinction from dust and the amount of dust is unknown. There are only three independent infrared hydrogen ratios, so the model must be limited to fitting to two parameters. Since the ratios are fairly constant with the lower limit on the ionization parameter, $\log U_{\text{min}} = -5.5$ is fixed, and Φ_{min} and n_{max} are free parameters.

The measured emission line ratios of four objects: J005812+160201, J010226–003904, J015950+002340, and J032213+005513 were used to find the most likely set of Φ_{min} and n_{max} limits by minimizing χ^2 :

$$\chi^2 = \sum_{i=1}^N \frac{(R_{\text{obs},i} - R_{\text{model},i})^2}{\sigma_{\text{stat},i}^2 + \sigma_{\text{sys},i}^2}, \quad (5)$$

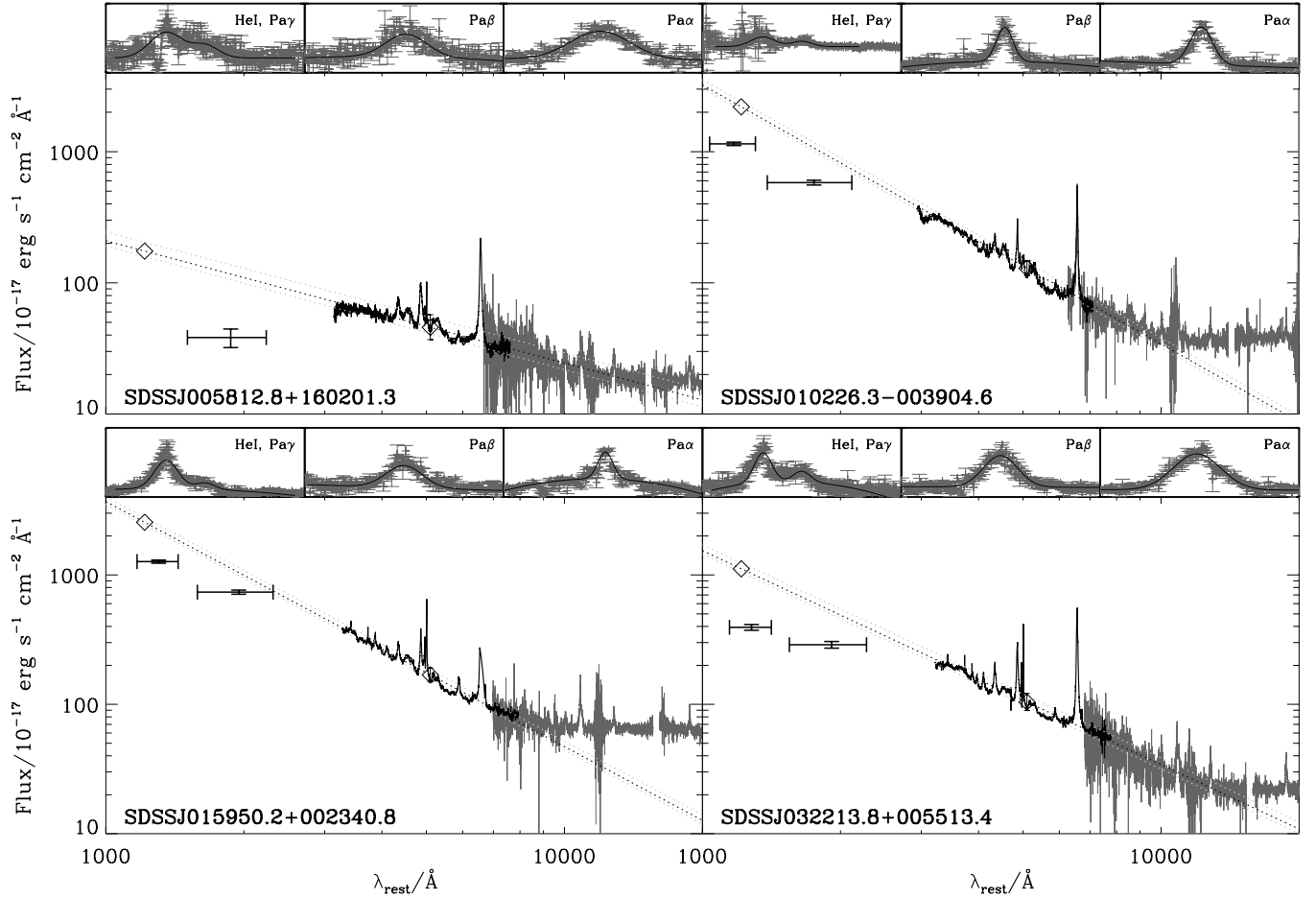


Figure 2. Glikman NIR spectra (dark gray), scaled SDSS spectra (black), *GALEX* far- and near-UV measurements (error bars). The extrapolated optical continuum (dotted line) is also shown, with an estimate of the 1216 Å continuum flux marked with a diamond. The insets show closeups of the Pa γ +He I 1.083 μ , Pa β , and Pa α emission lines with best-fit Gaussians.

Table 3
Measured and Predicted Ratios

Object	χ^2	Used for Fit						Not Used for Fit					
		Pa α /Pa β		Pa γ /Pa β		H α /Pa β		H α /H β		H γ /H β		He I 1.0830/H I 5876	
		m	p	m	p	m	p	m	p	m	p	m	p
J005812+160201	1.5	1.29 \pm 0.2	1.34	0.58 \pm 0.1	0.74	10.6 \pm 2.2	10.6	2.62 \pm 0.4	3.04	0.29 \pm 0.1	0.53	4.54 \pm 0.8	3.09
J010226-003904 ^d	0.27	1.21 \pm 0.2	1.18	0.92 \pm 0.1	0.86	13.1 \pm 2.0	13.4	2.87 \pm 0.4	3.18	0.41 \pm 0.1	0.46	4.41 \pm 0.7	2.42
J015950+002340	3.1	1.32 \pm 0.2	1.30	0.62 \pm 0.1	0.74	6.40 \pm 3.0	10.3	1.79 \pm 0.9	2.90	0.57 \pm 0.1	0.55	2.13 \pm 0.3	2.96
J032213+005513 ^d	0.90	1.36 \pm 0.2	1.44	0.65 \pm 0.1	0.73	12.8 \pm 2.2	12.8	2.89 \pm 0.4	3.60	0.49 \pm 0.1	0.45	3.23 \pm 0.5	3.23

Notes. Measured (m) and predicted (p) broad emission line flux ratios. Using the best-fit parameters discussed in Section 4.1, the H α /H β , H γ /H β , and He I 1.083 μ /He I λ 5876 ratios were predicted for each object. The predicted ratios are compared to the measured SDSS ratios. A 10% systematic was included in each measured flux. Objects that are in the Dong et al. (2008) sample are denoted by *d*.

where R_{obs} and R_{model} are the observed and predicted ratios, and σ_{stat} and σ_{sys} are the statistical and systematic uncertainties on each measured ratio. The sum is over each ratio used to find the best model: Pa α /Pa β , Pa γ /Pa β , and H α /Pa β . R_{model} is the predicted ratio for each combination of Φ_{min} and n_{max} values calculated using Equation (3), over the ranges given in Equation (4). Table 3 shows the minimum χ^2 value for each object. Figure 3 shows the χ^2 contours for each object in the Φ_{min} - n_{max} plane. This plot shows that the χ^2 value is minimized where the density upper integration limit is high and the lower limit on the ionizing flux is low.

Figure 4 shows the best-fit simulated ratios as a function of the two free parameters: n_{max} and Φ_{min} . The best-fit n_{max} and

Φ_{min} limits are given in the legend for each object. The n_{min} and Φ_{max} integration limits were fixed at fiducial values given in Section 2.4. The measured infrared ratios are overplotted as a band, indicating a 1σ uncertainty. Note that the He I 1.083 μ /Pa β ratio was not used as a constraint, as this ratio predicts Φ_{min} and n_{max} values that are systematically offset from those given by the hydrogen line ratios, as shown in Figure 4.

4.2. Predicted Balmer Ratios

The limits on n_{max} and Φ_{min} that were calculated by analyzing the NIR emission lines were then used to predict H α /H β and H γ /H β ratios. The predicted ratios are shown with the measured ratios in Table 3. Two of the four objects are in the Dong et al.

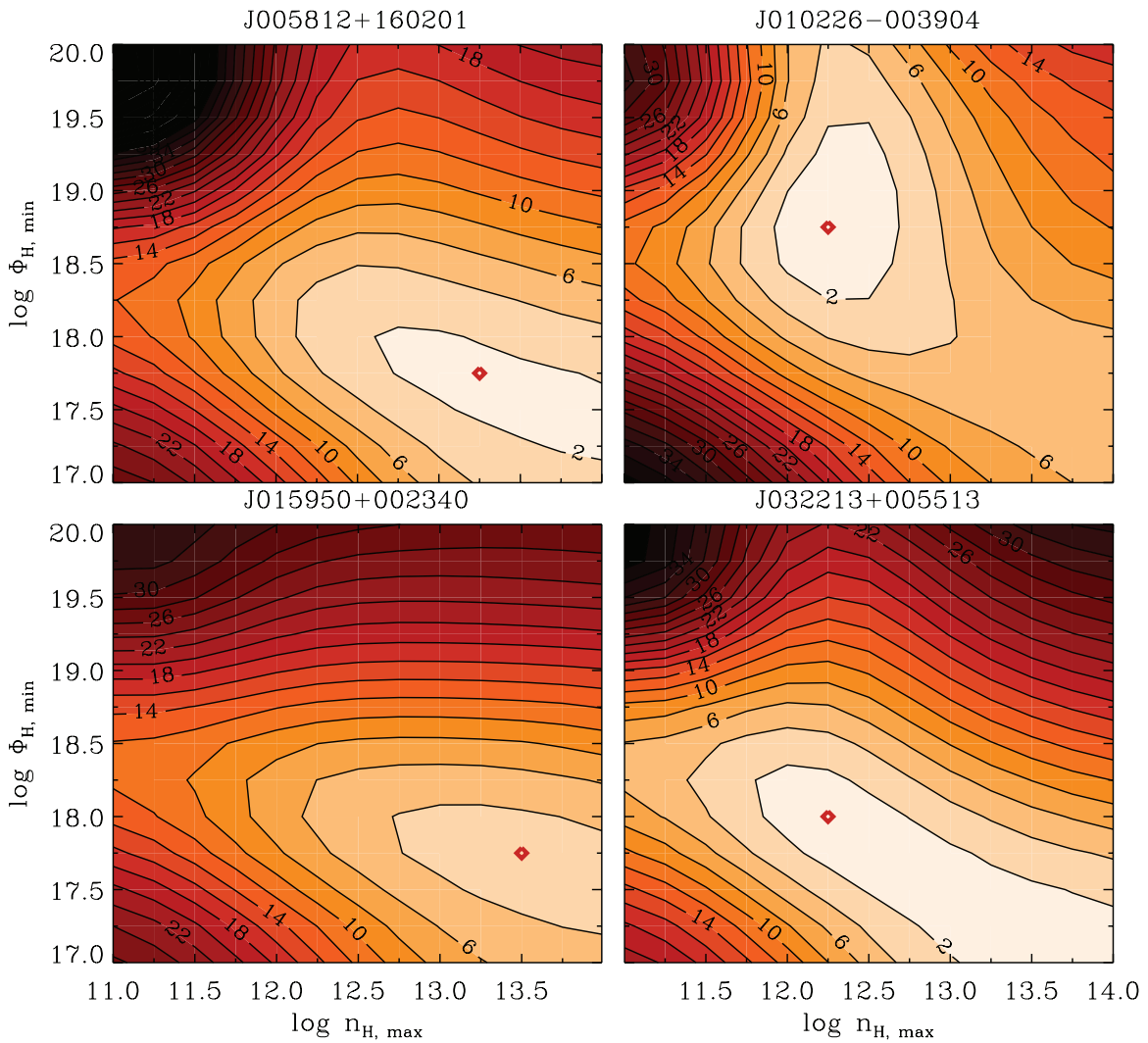


Figure 3. Contours of reduced χ^2 in the Φ_{\min} - n_{\max} plane for each of the four objects. Measured $\text{Pa}\alpha/\text{Pa}\beta$, $\text{Pa}\gamma/\text{Pa}\beta$, and $\text{H}\alpha/\text{Pa}\beta$ ratios were used to calculate χ^2 . In each panel, the location of the minimum χ^2 is shown with a red diamond (see Table 3 for minimum values of reduced χ^2).

(A color version of this figure is available in the online journal.)

(2008) sample, which selected AGNs with blue optical continua in order to minimize the effect of dust extinction. If blue continua do indicate less dust along the line of sight, the simulated ratios should be in good agreement with the measured ratios for these objects. This is true for the two objects listed, however, a much larger sample with a larger number of ratios studied is required to test this hypothesis. J015950+002340 also has a blue continuum, however simulated values cannot be compared to measurements, due to the poor fit to the $\text{H}\alpha$ line.

For all objects, the predicted Balmer decrements are slightly larger than the measured values, which is the opposite effect to dust. However, the predicted values are within measurement uncertainties, which may indicate that there is little internal reddening in these objects. The predicted $\text{H}\gamma/\text{H}\beta$ ratios are consistent with the measured data. The results for each object are summarized briefly in Section 4.5.

4.3. The Predicted $\text{Ly}\alpha/\text{H}\beta$ and UV Line Ratios

Although UV emission lines have not been measured for these objects, a selection of predicted UV emission line ratios is presented in this section. Typical measured strengths of stronger

UV lines were compared to the predicted values to check the consistency of our spectral model derived from the measured hydrogen spectrum. We note that the UV metal emission line strengths depend more on the shape of the incident ionizing continuum (and to varying degrees the gas metallicity) than do the Balmer and Paschen hydrogen lines under study (e.g., see Korista et al. 1998 for a discussion). The predicted UV emission line strengths reported here are those that result from the best fit in the physical parameters (n_{\max} , Φ_{\min}) determined from the three hydrogen emission line ratios (as noted in Table 3) in each of the four AGNs.

Predicted $\text{Ly}\alpha/\text{H}\beta$ ratios for each object are listed in Table 4. Most of the $\text{Ly}\alpha/\text{H}\beta$ predicted ratios are lower than the simple, classical photoionization prediction (Osterbrock & Ferland 2006). This is because of the inclusion of high-density gas. $\text{Ly}\alpha$ thermalizes at high densities, whereas the Balmer lines continue to emit efficiently, causing the predicted $\text{Ly}\alpha/\text{H}\beta$ ratio to decrease with the inclusion of high n_{H} gas. Nevertheless, these ratios remain larger than many of those measured in AGNs, and this remains an unsolved problem. However, uncorrected extinction due to grains extrinsic to the Milky Way may explain much of the remaining discrepancies (see Netzer et al. 1995).

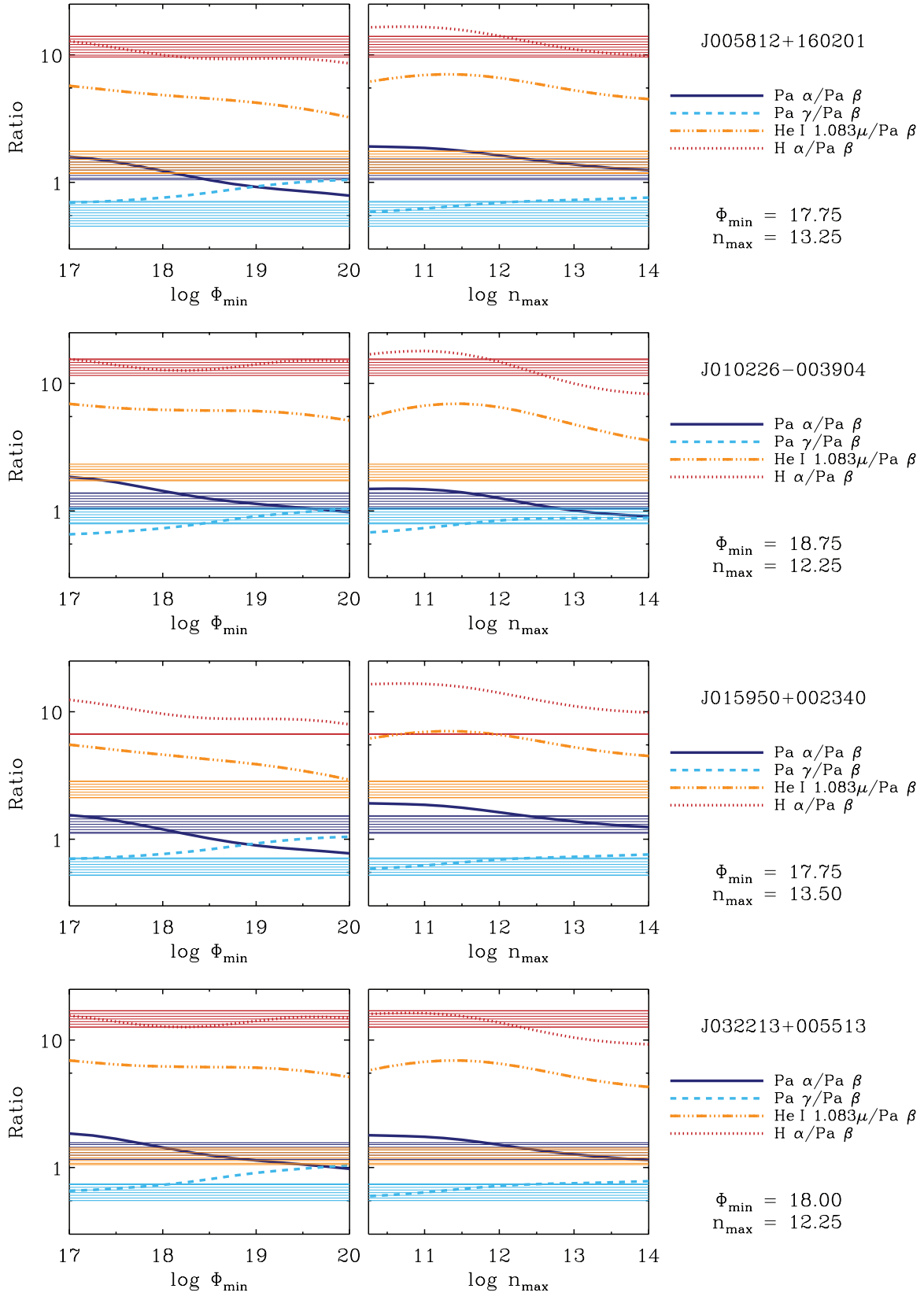


Figure 4. Measured ratios are plotted compared to the best-fit models. The solid, dashed, dot-dashed, and dotted lines show the simulated $\text{Pa } \alpha / \text{Pa } \beta$, $\text{Pa } \gamma / \text{Pa } \beta$, $\text{He I } 1.083 \mu / \text{Pa } \beta$, and $\text{H } \alpha / \text{Pa } \beta$ ratios, respectively. The measured values are shown as a band with 1σ uncertainties in a corresponding color. For legibility, the very large $\text{H } \alpha$ measurement uncertainty is not shown for J015950+002340, although it was used in the best-fit calculation. The parameters that produce the best fit for each object have been plotted and the values are given in the legend for each object. Note that a log scale has been used on the y-axis, so that the range of ratios can easily be seen.

(A color version of this figure is available in the online journal.)

Table 4
Predicted Ly α /H β and Ultraviolet Line Ratios

Object	Ly α /H β	O VI+Ly β /Ly α	C IV/Ly α	Mg II/Ly α
J005812+160201	19	0.14	0.33	0.22
J010226–003904	40	0.24	0.40	0.09
J015950+002340	17	0.14	0.33	0.22
J032213+005513	31	0.16	0.35	0.16
Measured ^a	12	0.10	0.25	0.14

Notes. Predicted Ly α /H β , and O VI λ 1035+Ly β , C IV λ 1549, and Mg II λ 2800 line ratios relative to Ly α . The line ratios were predicted using the best-fit parameters derived in Section 4.1.

^a The measured line ratios are from the Vanden Berk et al. (2001) composite spectrum.

A selection of predicted UV metal lines (relative to Ly α) is listed in Table 4. These lines were chosen as they are relatively strong, and they span a large range in ionization parameter. The O VI, C IV, and Mg II emission lines are also the most important coolants within their ionization zones (excepting emission by Fe II). As these lines are major coolants, the line strengths are not very sensitive to the gas metallicity, due to the thermostatic effects of such lines. The predicted C IV values are somewhat higher than the ratio measured from the Vanden Berk et al. (2001) composite spectrum, however, the predicted C IV/Ly α ratio is strongly dependent on the hardness of the ionizing continuum. The observed value shows significant variation; for example, the C IV/Ly α ratio is 0.62 in the Zheng et al. (1997) composite, and is closer to 1 in Seyfert 1 spectra (Korista & Goad 2000; see also Osmer et al. 1994). Although additional free parameters, such as metallicity and the shape of the ionizing continuum, have not been considered here, the predicted strengths of the UV metal lines relative to Ly α are generally consistent with typical measured values.

4.4. Do the Models Produce Enough Energy?

A simple check, albeit with a substantial uncertainty, can establish whether the best-fit models produce enough energy to reproduce the observed total integrated line flux. The largest uncertainty in comparing measured equivalent width values to predicted line strengths is knowing which continuum flux to compare the line flux to. The NIR continuum is a poor indicator of the incident ionizing continuum (i.e., photons with wavelengths shorter than 912 Å), and is contaminated with hot thermal dust emission as well as that of the host galaxy. To test whether the models produce enough energy, the predicted and measured Pa β equivalent widths were compared, relative to two different points in the continuum: 1216 Å and 5100 Å. Note that the predicted equivalent width depends on the integrated covering factor. In this section, the integrated covering factor was calculated such that the simulated equivalent width of Ly α is 100 Å. This is a typical measured value for $W_{1216}(\text{Ly}\alpha)$, and was chosen to ensure that the model produces enough energy to be consistent with the observed value. For each object, this value of f_c was used to calculate all equivalent width values presented in this section.

The equivalent width relative to the continuum flux at 1216 Å is often chosen because it is easily observable and close to the ionizing continuum. Contaminants such as light from the host galaxy and dusty torus are negligible in this region. The measured value was estimated using both the GALEX and SDSS UV continuum flux values (S_{1216}) listed in Table 2. The observed

Table 5
Predicted Rest-frame Equivalent Width of Pa β

Object	$W_{1216}(\text{Pa } \beta)$			$W_{5100}(\text{Pa } \beta)$		f_c
	GALEX	SDSS	p	SDSS	p	
J005812+160201	...	10	1.5	30	12	0.31
J010226–003904 ^d	0.3	0.3	0.57	6	4.5	0.41
J015950+002340	0.7	0.6	1.7	10	13.3	0.32
J032213+005513 ^d	2	1	0.89	10	7.1	0.30

Notes. Measured and predicted (p) Pa β equivalent width values (in Å) normalized to two different points in the continuum: 1216 Å (SDSS and GALEX) and 5100 Å (SDSS only). The predicted equivalent width values are calculated using the best-fit parameters and were scaled using an integrated covering fraction that gives a predicted Ly α equivalent width of 100 Å. The value of f_c required to produce $W_{1216}(\text{Ly}\alpha) = 100$ Å is also given. Uncertainties on the measured equivalent width values are large, and these values are estimated to be accurate to a factor of ~ 2 .

rest-frame equivalent width of Pa β relative to the incident continuum at 1216 Å (in Å) is given by

$$W_{1216}(\text{Pa } \beta) = \frac{F(\text{Pa } \beta)}{S_{1216}} \times \frac{1}{(1+z)}, \quad (6)$$

where S_{1216} is the measured incident continuum flux at 1216 Å and $F(\text{Pa } \beta)$ is the total integrated emission line flux, given in Table 1. The dominant measurement uncertainties are quasar variability and scaling the UV measurement to the NIR. There is an additional uncertainty from dust attenuation. The measured S_{1216} values show a large variance between the GALEX and SDSS estimates, therefore this value is estimated to be accurate within a factor of two.

The measured Pa β equivalent width value relative to the incident continuum at 5100 Å ($W_{5100}(\text{Pa } \beta)$) was also calculated. At this wavelength the continuum flux is directly measurable from the scaled SDSS spectrum (unlike the SDSS continuum at 1216 Å, which is an extrapolated estimate). However, the 5100 Å continuum is much further from the ionizing continuum and host galaxy contamination is not negligible at this wavelength, making it a poorer proxy for the ionizing continuum. There may also be some thermal emission from the BELR clouds and reflected light from the dusty torus contributing to the measured continuum flux at this wavelength. The calculation of $W_{5100}(\text{Pa } \beta)$ is analogous to the calculation of $W_{1216}(\text{Pa } \beta)$ given in Equation (6). Given the large uncertainties in scaling the continuum measurements to the NIR, quasar variability, and host galaxy contamination in the S_{5100} measurement, the measured values listed in Table 5 should only be considered accurate to within a factor of two.

Using the best-fit n_{max} and Φ_{min} integration limits determined in Section 4.1, the simulated $W_{1216}(\text{Pa } \beta)$ and $W_{5100}(\text{Pa } \beta)$ values were calculated for each object. Both measures of equivalent width can be output by Cloudy directly. (Note that these estimates assume the standard Cloudy continuum described in Section 2.1.) To compare the simulated equivalent width values to the measured values, predicted $W_{1216}(\text{Pa } \beta)$ and $W_{5100}(\text{Pa } \beta)$ values must be scaled by the integrated cloud covering fraction (f_c). For each object, the integrated covering fraction required to produce $W_{1216}(\text{Ly}\alpha) = 100$ Å (a typical value) was computed for the best-fit parameters. This value of f_c was then used to scale the predicted equivalent width values.

The measured and predicted $W_{1216}(\text{Pa } \beta)$ and $W_{5100}(\text{Pa } \beta)$ values, and the value of f_c are listed in Table 5. As shown in this table, the computed integrated covering fraction re-

quired to produce $W_{1216}(\text{Ly}\alpha) = 100 \text{ \AA}$ for each object is not unrealistically large. The measured and predicted $W_{1216}(\text{Pa}\beta)$ values are also in good agreement (with the exception of J005812+160201, which has a shallower UV continuum slope than the Cloudy AGN continuum). Therefore, Table 5 shows that the best-fit models produce enough energy to be consistent with both the measured $\text{Pa}\beta$ and previously observed $\text{Ly}\alpha$ equivalent width values.

4.5. Results for Each Object

A brief description of the results for each object is given below.

J005812+160201. The model is a good fit to the data, although the predicted $\text{H}\gamma/\text{H}\beta$ ratio is 2σ larger than the measured ratio. The measured $\text{H}\gamma/\text{H}\beta$ ratio is low compared with the other objects. The predicted total equivalent width barely produces enough energy to be consistent with the observations. The low predicted equivalent width of $\text{Pa}\beta$ is at least partially due the assumed Cloudy continuum, which is a poor approximation in this case, as the measured UV spectrum is much shallower than the Cloudy continuum. The measured $W_{1216}(\text{Pa}\beta)$ is high compared to the other objects, again because the continuum slope is very shallow.

J010226–003904. The model is a good fit to the data. This object has a strange broad absorption line (BAL)-like feature in $\text{He I } 1.083\mu$, probably due to the atmosphere. However, this feature could be real, similar to that reported by Leighly et al. (2011). The predicted Φ_{\min} value is quite high, which results from the large measured $\text{Pa}\gamma/\text{Pa}\beta$ ratio.

J015950+002340. The model is a fair fit to the data, as the reduced χ^2 value is 3.1. This source, also known as Mrk 1014, is an ultraluminous infrared galaxy (ULIRG; see Armus et al. 2004, and references therein). The $\text{H}\alpha$ emission line is highly asymmetric and is not well fit by a Gaussian, making comparisons to simulations difficult. The predicted high density could be a consequence of the underestimation of the $\text{H}\alpha$ flux. Note that the measured $\text{H}\alpha/\text{Pa}\beta$ and $\text{H}\alpha/\text{H}\beta$ ratios are low compared with the other objects. Also note that the optical and NIR He I line flux (relative to the hydrogen line flux) is high compared with the other objects.

J032213+005513. The model produced a good fit to the emission line ratios, although the predicted $\text{H}\alpha/\text{H}\beta$ ratio is 2σ above the measured value.

5. DISCUSSION

The predictions of Cloudy LOC models have been tested by comparing simulated ratios to measured near-infrared hydrogen emission line ratios. Near-infrared hydrogen emission lines were chosen to better understand hydrogen emission from the BELR, and because near-infrared ratios are insensitive to uncertainties in the line-of-sight extinction due to the presence of dust. The signal to noise of the published spectra is limited, so only four quasars were considered suitable. Two questions were considered.

1. Is a good fit to the observed line ratios possible using the LOC model?
2. What are the integration limits for the best-fit LOC models? Due to the limited number of independent line ratios, only two integration limits in the LOC model could be tested.

5.1. Can a Simple LOC Model Fit These Observations?

In three of the four cases, a good fit to the hydrogen emission lines is obtained by the LOC model. In the fourth case the fit is fair. In addition, the shape of the χ^2 contour distributions in the density–flux plane is similar for all objects. High Φ_{\min} limits are generally highly disfavored. This suggests that $\log \Phi_{\min} < 18$, and that low-incident-ionizing fluxes are required to reproduce observed hydrogen emission line flux ratios. The determined limits on Φ_{\min} are also consistent with the dust sublimation radius (Nenkova et al. 2008). This is in agreement with several recent studies that suggest the Balmer lines and Mg II in large part come from the outer BELR and near or at the dust sublimation radius (Zhu et al. 2009; Czerny & Hryniewicz 2011; Mor & Netzer 2012).

Figure 3 shows that lower n_{\max} values in combination with low Φ_{\min} values are also highly disfavored (i.e., χ^2 values are high in the lower left corner of the plot), meaning that BELRs with a low high-density cutoff and low low-incident-ionizing flux cutoff are unlikely solutions. The minimum of the χ^2 contours tend to lie on a diagonal in the n_{\max} – Φ_{\min} plane: if n_{\max} is larger, then Φ_{\min} is smaller. If the BELR includes regions where the incident ionizing flux is very low, then gas with a very high number density is required to reproduce the observed emission line ratios. This solution is quite unlikely though, as dust grains condense at low Φ_{H} , destroying the line emission. The validity of the inferred limits is uncertain. A larger sample, with higher signal to noise is required to test these results.

The predicted $\text{H}\alpha/\text{H}\beta$ and $\text{H}\gamma/\text{H}\beta$ ratios are generally in very good agreement with the measured ratios, as shown in Table 3. However, the measured $\text{He I } 1.083\mu/\text{Pa}\beta$ ratio does not match the simple LOC model described here. We also find that the predicted $\text{He I } 5876/\text{H}\beta$ line ratio is significantly higher than the measured values. The simulated values are typically a factor of ~ 2 greater than the measured values. This offset could be caused by the simplicity of the covering fractions assumed in this model. The shape of the $W_{1216}(\text{He I } 1.083\mu)$ contours is quite different to the Balmer and Paschen lines, making ratios involving $\text{He I } 1.083\mu$ more sensitive to the power laws assumed in Equation (2). Although the slope of the power laws is not expected to deviate significantly from -1 , refinement of the models using different power-law distributions in $f(r)$ and $g(n_{\text{H}})$ will be the subject of future studies. The predicted overestimate of both the $\text{He I } \lambda 5876/\text{H}\beta$ and $1.083\mu/\text{Pa}\beta$ line ratios could also indicate that Cloudy overpredicts the He I emission spectrum relative to H.

5.2. Dust

The amount of attenuation from internal dust (i.e., dust within the host galaxy) is unknown. The Balmer decrement is the most widely measured ratio is AGN spectroscopy (e.g., Osterbrock 1977; Groves et al. 2012), and has long been used as an indicator of the amount of extinction (e.g., Berman 1936). Dong et al. (2008) measured the Balmer decrement for a sample of 446 Seyfert 1s and QSOs with blue continua, which were selected to minimize the effect of dust extinction. They found only a small intrinsic scatter in the measured ratio, which suggests that the intrinsic Balmer decrement could be relatively consistent between objects, and the observed variance is due to different amounts of dust along the line of sight within the host galaxy. However, this result relies on the slope of the continuum being a dust indicator (see Davis et al. 2007 for a discussion).

The continua of our subset of quasars are reasonably blue, with the exception of J005812+160201. If dust attenuation caused reddening of the continuum in this case, a larger observed $H\alpha/H\beta$ would be expected. Unfortunately, it is not possible to test this assertion with such a limited sample size. The presence of uncorrected extinction due to dust along the line of sight would also increase the observed $\text{He I } 1.083/\text{He I } 5876$ ratio above that of the predicted one (see Table 3).

With better quality spectra, an estimate of the amount of dust attenuation could be made. The $\text{Ly}\alpha/H\beta$ problem could be at least partially explained by internal extinction (Shuder & MacAlpine 1979) and constraining the amount of dust attenuation is important to resolve this matter.

5.3. Composite Quasar Spectra

The value of the $\text{Pa}\alpha/\text{Pa}\beta$ line ratio measured from the Glikman et al. (2006) composite spectrum was 0.64 ± 0.01 . However, this value is much lower than the values measured from individual objects, which are consistently above 1.0 (see Table 3). Other observed $\text{Pa}\alpha/\text{Pa}\beta$ emission line ratios in quasars are consistent with this result (e.g., Soifer et al. 2004, who measured a $\text{Pa}\alpha/\text{Pa}\beta$ ratio of 1.05 ± 0.2 in a $z = 3.91$ quasar). Ratios of $\text{Pa}\alpha/\text{Pa}\beta$ that are above 1.0 have also been measured in lower-luminosity AGNs (Landt et al. 2008).

While it is possible that systematic effects cause objects with larger $\text{Pa}\alpha/\text{Pa}\beta$ ratios to be preferentially selected in our sample, a bias caused by the composite methodology is a more likely explanation. Composite spectra are useful for describing generic properties of a sample and for identifying emission lines that are too weak to be observed in individual spectra. However, care must be taken in ascribing physical significance to individual features of composite spectra. It is not clear whether composite spectra are useful for investigating detailed physical properties of the line-emitting gas. Emission line ratios in the composite spectrum can also be affected by poor S/Ns of individual spectra, and wavelength ranges where there are few objects contributing to the final spectrum. See Sulentic et al. (2002) for a discussion of how emission line ratios are affected, and an alternative method for producing composite spectra.

5.4. Caveats

The NIR spectroscopy was not simultaneous with the optical and UV measurements. As quasars are intrinsically variable, this will introduce a systematic uncertainty. Even after continuum matching, the line fluxes will be altered; this effect is known as the intrinsic Baldwin effect (e.g., Pogge & Peterson 1992). There is often a considerable difference between *GALEX* and SDSS S_{1216} values. The objects in Table 2 SDSS are all observed during 2000. NIR observations are from 2003 September to 2004 September and *GALEX* observations are in 2003 (and one in 2005).

Fitting the emission lines with Gaussians introduces another systematic uncertainty. Glikman et al. (2006) point out that Gaussians do not fit the broad wings well; however, Gaussians generally fit the bulk of the broad emission line flux, while requiring only a small number of free parameters. The estimated contribution from the narrow component is less than 5%. Dong et al. (2008) deconvolved the emission lines into both a broad and narrow component, and in each case the equivalent width of the narrow component is only a few percent of the broad component. Fe II contamination was not considered. Fitting the

Fe II contamination would introduce additional errors, given the low signal to noise of the data.

Fixing the lower limit on the ionization parameter, U_{\min} is not ideal, however, the ratios considered are insensitive to U_{\min} and with only a few measured ratios, the model must be limited in complexity. The U_{\min} limit would be better determined with the Ca II infrared triplet (Ca II XYZ) or other U_{\min} -sensitive ratios (see A. J. Ruff et al. 2012, in preparation for a discussion). Single point solutions in the density–flux plane were not considered for reasons discussed in Section 2.2.

Since the Balmer and Paschen lines are optically thick, the geometry will affect the predicted emission. If the BELR geometry is such that emission from the “back” of the clouds is not observed, the predicted emission line ratios will change (Ferland et al. 1992; O’Brien et al. 1994; A. J. Ruff et al. 2012, in preparation).

Any broad emission line flux measurement is from a snapshot in time. The ratios will vary with time as the continuum luminosity varies, and this will be dependent on the distribution of the gas—both in geometry and physical state. Comparing measured flux ratios can be problematic if the source is highly variable and lines are formed at very different radii. The recombination lines are emitted relatively efficiently over a broad range of physical conditions, and their continuum reprocessing efficiencies are largely dependent on the incident flux, and therefore the distance from the ionizing source, due to optical depths in the excited states (Korista et al. 1997; A. J. Ruff et al. 2012, in preparation). This manifests in different measured reverberation mapping signals and line profile variability (e.g., Sergeev et al. 2001; Kollatschny & Zetzl 2010). For example, not only do the Balmer lines show different measured time lags, but the line responsivity is observed to decrease from line center to line wing (see Korista & Goad 2004, for a discussion). This could be corrected for if the distribution of broad emission line gas could be determined using high-quality spectral and temporal data in conjunction with photoionization models (Horne et al. 2003).

6. SUMMARY

We have demonstrated a new diagnostic for the density and ionization state of the hydrogen broad-line gas in quasars. The results should be seen as preliminary, being based on fairly low S/N ($\approx 10 \text{ pixel}^{-1}$ in the continuum) data for a small number of objects. The technique is promising because the hydrogen line ratios depend strongly on the physical conditions, but weakly on metallicity, column density, and slope of the ionizing continuum. The ionizing flux is a good measure of distance from the source, and the technique offers an alternative route to measuring the structure of the quasar central engine, in addition to the physical state of the broad-line gas.

Despite the simplicity of the model, broad NIR hydrogen emission line ratios can be reproduced by an LOC integration. All hydrogen ratios predicted, including the Balmer decrement, were consistent with those observed. Low-incident-ionizing flux values ($\Phi_{\text{H}} < 10^{18} \text{ cm}^{-2} \text{ s}^{-1}$) are required to reproduce the observed hydrogen emission line ratios. This predicted lower limit on Φ_{H} gives an outer radius of the BELR that is consistent with the radius of dust sublimation calculated by Nenkova et al. (2008).

This model predicts that high number density gas ($n_{\text{H}} > 10^{12} \text{ cm}^{-3}$) is required to reproduce the observed hydrogen emission line ratios. The upper limit on the gas number density is high compared with previous calculations, however, all predictions stated here should be considered estimates, because

of the simplicity of the model and limitations in the quality and number of spectra.

With a larger sample of high signal-to-noise quasar spectra in the NIR, higher order lines in the Paschen series could also be observed. More constraints on the parameter space and other free parameters will be included in the model.

A.J.R. acknowledges the support of an Australian Postgraduate Award. We are grateful to Gary Ferland and collaborators for freely distributing and maintaining the photoionization code, Cloudy. We thank Eilat Glikman et al. for making their near-infrared spectra publicly available. This research has made use of the NASA/IPAC Extragalactic Database (NED) which is operated by the Jet Propulsion Laboratory, California Institute of Technology, under contract with the National Aeronautics and Space Administration.

The Infrared Telescope Facility (IRTF) is operated by the University of Hawaii under Cooperative Agreement no. NNX-08AE38A with the National Aeronautics and Space Administration, Science Mission Directorate, Planetary Astronomy Program.

Funding for the SDSS and SDSS-II has been provided by the Alfred P. Sloan Foundation, the Participating Institutions, the National Science Foundation, the U.S. Department of Energy, the National Aeronautics and Space Administration, the Japanese Monbukagakusho, the Max Planck Society, and the Higher Education Funding Council for England. The SDSS Web site is <http://www.sdss.org/>. The SDSS is managed by the Astrophysical Research Consortium for the Participating Institutions. The Participating Institutions are the American Museum of Natural History, Astrophysical Institute Potsdam, University of Basel, University of Cambridge, Case Western Reserve University, University of Chicago, Drexel University, Fermilab, the Institute for Advanced Study, the Japan Participation Group, Johns Hopkins University, the Joint Institute for Nuclear Astrophysics, the Kavli Institute for Particle Astrophysics and Cosmology, the Korean Scientist Group, the Chinese Academy of Sciences (LAMOST), Los Alamos National Laboratory, the Max-Planck-Institute for Astronomy (MPIA), the Max-Planck-Institute for Astrophysics (MPA), New Mexico State University, Ohio State University, University of Pittsburgh, University of Portsmouth, Princeton University, the United States Naval Observatory, and the University of Washington.

GALEX is operated for NASA by the California Institute of Technology under NASA contract NAS5-98034.

REFERENCES

- Arav, N., Barlow, T. A., Laor, A., Sargent, W. L. W., & Blandford, R. D. 1998, *MNRAS*, **297**, 990
- Armus, L., Charmandaris, V., Spoon, H. W. W., et al. 2004, *ApJS*, **154**, 178
- Baldwin, J., Ferland, G., Korista, K., & Verner, D. 1995, *ApJ*, **455**, L119
- Baldwin, J. A. 1977, *MNRAS*, **178**, 67P
- Baldwin, J. A., Ferland, G. J., Korista, K. T., Hamann, F., & LaCluyzé, A. 2004, *ApJ*, **615**, 610
- Bate, N. F., Floyd, D. J. E., Webster, R. L., & Wyithe, J. S. B. 2008, *MNRAS*, **391**, 1955
- Berman, L. 1936, *MNRAS*, **96**, 890
- Blandford, R. D., & McKee, C. F. 1982, *ApJ*, **255**, 419
- Bottomoff, M., Ferland, G., Baldwin, J., & Korista, K. 2000, *ApJ*, **542**, 644
- Bottomoff, M. C., Baldwin, J. A., Ferland, G. J., Ferguson, J. W., & Korista, K. T. 2002, *ApJ*, **581**, 932
- Collin-Souffrin, S., Dumont, S., & Tully, J. 1982, *A&A*, **106**, 362
- Czerny, B., & Hryniewicz, K. 2011, *A&A*, **525**, L8
- Davidson, K. 1972, *ApJ*, **171**, 213
- Davidson, K. 1977, *ApJ*, **218**, 20
- Davidson, K., & Netzer, H. 1979, *Rev. Mod. Phys.*, **51**, 715
- Davis, S. W., Woo, J.-H., & Blaes, O. M. 2007, *ApJ*, **668**, 682
- Dong, X., Wang, T., Wang, J., et al. 2008, *MNRAS*, **383**, 581
- Emmering, R. T., Blandford, R. D., & Shlosman, I. 1992, *ApJ*, **385**, 460
- Ferguson, J. W., & Ferland, G. J. 1997, *ApJ*, **479**, 363
- Ferguson, J. W., Korista, K. T., Verner, D. A., & Ferland, G. J. 2001, in ASP Conf. Ser. 247, Spectroscopic Challenges of Photoionized Plasmas, ed. G. Ferland & D. W. Savin (San Francisco, CA: ASP), **287**
- Ferland, G. J., Fabian, A. C., Hatch, N. A., et al. 2009, *MNRAS*, **392**, 1475
- Ferland, G. J., Korista, K. T., Verner, D. A., et al. 1998, *PASP*, **110**, 761
- Ferland, G. J., Netzer, H., & Shields, G. A. 1979, *ApJ*, **232**, 382
- Ferland, G. J., & Persson, S. E. 1989, *ApJ*, **347**, 656
- Ferland, G. J., Peterson, B. M., Horne, K., Welsh, W. F., & Nahar, S. N. 1992, *ApJ*, **387**, 95
- Fitzpatrick, E. L. 1999, *PASP*, **111**, 63
- Glikman, E., Helfand, D. J., & White, R. L. 2006, *ApJ*, **640**, 579
- Groves, B., Brinchmann, J., & Walcher, C. J. 2012, *MNRAS*, **419**, 1402
- Horne, K., Korista, K. T., & Goad, M. R. 2003, *MNRAS*, **339**, 367
- Joly, M. 1989, *A&A*, **208**, 47
- Kim, D., Im, M., & Kim, M. 2010, *ApJ*, **724**, 386
- Kollatschny, W., & Zetzl, M. 2010, *A&A*, **522**, A36
- Kollatschny, W., & Zetzl, M. 2011, *Nature*, **470**, 366
- Korista, K., Baldwin, J., & Ferland, G. 1998, *ApJ*, **507**, 24
- Korista, K., Baldwin, J., Ferland, G., & Verner, D. 1997, *ApJS*, **108**, 401
- Korista, K. T., & Goad, M. R. 2000, *ApJ*, **536**, 284
- Korista, K. T., & Goad, M. R. 2004, *ApJ*, **606**, 749
- Krolik, J. H., Horne, K., Kallman, T. R., et al. 1991, *ApJ*, **371**, 541
- Kwan, J., & Krolik, J. H. 1981, *ApJ*, **250**, 478
- Landt, H., Bentz, M. C., Ward, M. J., et al. 2008, *ApJS*, **174**, 282
- Laor, A. 2006, *ApJ*, **643**, 112
- Leighly, K. M., Dietrich, M., & Barber, S. 2011, *ApJ*, **728**, 94
- Mathews, W. G., & Ferland, G. J. 1987, *ApJ*, **323**, 456
- Matsuoka, Y., Oyabu, S., Tsuzuki, Y., & Kawara, K. 2007, *ApJ*, **663**, 781
- Mor, R., & Netzer, H. 2012, *MNRAS*, **420**, 526
- Nagao, T., Marconi, A., & Maiolino, R. 2006, *A&A*, **447**, 157
- Neenkova, M., Sirocky, M. M., Nikutta, R., Ivezić, Ž., & Elitzur, M. 2008, *ApJ*, **685**, 160
- Netzer, H., Brotherton, M. S., Wills, B. J., et al. 1995, *ApJ*, **448**, 27
- Netzer, H., & Laor, A. 1993, *ApJ*, **404**, L51
- O'Brien, P. T., Goad, M. R., & Gondhalekar, P. M. 1994, *MNRAS*, **268**, 845
- O'Dowd, M., Bate, N. F., Webster, R. L., Wayth, R., & Labrie, K. 2011, *MNRAS*, **415**, 1985
- Osmer, P. S., Porter, A. C., & Green, R. F. 1994, *ApJ*, **436**, 678
- Osterbrock, D., & Ferland, G. J. 2006, *Astrophysics of Gaseous Nebulae and Active Galactic Nuclei* (Mill Valley, CA: University Science Books)
- Osterbrock, D. E. 1970, *ApJ*, **160**, 25
- Osterbrock, D. E. 1977, *ApJ*, **215**, 733
- Osterbrock, D. E., & Mathews, W. G. 1986, *ARA&A*, **24**, 171
- Peterson, B. M. 1994, in ASP Conf. Ser. 69, Reverberation Mapping of the Broad-Line Region in Active Galactic Nuclei, ed. P. M. Gondhalekar, K. Horne, & B. M. Peterson (San Francisco, CA: ASP), **1**
- Peterson, B. M. 2011, arXiv:1109.4181
- Pogge, R. W., & Peterson, B. M. 1992, *AJ*, **103**, 1084
- Porter, R. L., Bauman, R. P., Ferland, G. J., & MacAdam, K. B. 2005, *ApJ*, **622**, L73
- Porter, R. L., & Ferland, G. J. 2007, *ApJ*, **664**, 586
- Rees, M. J., Netzer, H., & Ferland, G. J. 1989, *ApJ*, **347**, 640
- Schlegel, D. J., Finkbeiner, D. P., & Davis, M. 1998, *ApJ*, **500**, 525
- Sergeev, S. G., Pronik, V. I., & Sergeeva, E. A. 2001, *ApJ*, **554**, 245
- Shuder, J. M., & MacAlpine, G. M. 1979, *ApJ*, **230**, 348
- Soifer, B. T., Charmandaris, V., Brandl, B. R., et al. 2004, *ApJS*, **154**, 151
- Sulentic, J. W., Marziani, P., Zamanov, R., et al. 2002, *ApJ*, **566**, L71
- Vanden Berk, D. E., Richards, G. T., Bauer, A., et al. 2001, *AJ*, **122**, 549
- Verner, E. M., Verner, D. A., Korista, K. T., et al. 1999, *ApJS*, **120**, 101
- Zheng, W., Kriss, G. A., Telfer, R. C., Grimes, J. P., & Davidsen, A. F. 1997, *ApJ*, **475**, 469
- Zhu, L., Zhang, S. N., & Tang, S. 2009, *ApJ*, **700**, 1173